Modeling of microwave-induced plasma in argon at atmospheric pressure

M. Baeva,[*] A. Bösel,[†] J. Ehlbeck,[‡] and D. Loffhagen[§]
Leibniz Institute for Plasma Science and Technology, INP Greifswald, Felix-Hausdorff-Straße 2, D-17489 Greifswald, Germany
(Received 29 February 2012; published 15 May 2012)

A two-dimensional model of microwave-induced plasma (field frequency 2.45 GHz) in argon at atmospheric pressure is presented. The model describes in a self-consistent manner the gas flow and heat transfer, the in-coupling of the microwave energy into the plasma, and the reaction kinetics relevant to high-pressure argon plasma including the contribution of molecular ion species. The model provides the gas and electron temperature distributions, the electron, ion, and excited state number densities, and the power deposited into the plasma for given gas flow rate and temperature at the inlet, and input power of the incoming TEM microwave. For flow rate and absorbed microwave power typical for analytical applications (200–400 ml/min and 20 W), the plasma is far from thermodynamic equilibrium. The gas temperature reaches values above 2000 K in the plasma region, while the electron temperature is about 1 eV. The electron density reaches a maximum value of about 4×10^{21} m^{-3}. The balance of the charged particles is essentially controlled by the kinetics of the molecular ions. For temperatures above 1200 K, quasineutrality of the plasma is provided by the atomic ions, and below 1200 K the molecular ion density exceeds the atomic ion density and a contraction of the discharge is observed. Comparison with experimental data is presented which demonstrates good quantitative and qualitative agreement.

DOI: 10.1103/PhysRevE.85.056404 PACS number(s): 52.40.Fd, 52.50.Dg, 52.80.Pi, 52.65.−y

I. INTRODUCTION

Microwave plasmas are often of particular interest due to their ability to provide a high density of charged particles and active species. Oscillating electromagnetic fields make direct measurements inside the microwave cavity unfeasible. Instead, nonintrusive optical measurements and numerical modeling are used to obtain the plasma parameters. Although microwave plasmas have been widely used in industry and research, to the best of our knowledge only a few two-dimensional (2D) self-consistent models of microwave-induced plasma exist. Calculation of the electromagnetic field applying frequency domain algorithm has been used in Refs. [1,2] assuming that the distributions of the plasma parameters are known. A 2D plasma model composed of a fluid model, a collisional radiative model, and an electromagnetic model has been presented in Ref. [3]. It describes microwave argon plasmas at pressure of 5 Torr by an iterative coupling and a grid interpolation. A 2D model of a low-pressure (100 Pa) linearly extended plasma source is given in Ref. [4], solving for the electromagnetic field, particle, and electron energy. An equilibrium microwave atmospheric pressure argon discharge in a coaxial waveguide with a truncated inner electrode has been simulated in Ref. [5], where the species densities are obtained from the Saha equation, the Dalton law, and the condition of quasineutrality. A two-temperature modeling of a microwave argon plasma jet has been reported in Ref. [6] where the electromagnetic field has been solved in a part of the computational domain and has been iteratively coupled to the fluid model. Modular modeling strategy has been followed in Refs. [7,8] to achieve an integrated description of a microwave-driven axial injection torch operated at atmospheric pressure in different gases and a wide range of power and flow rate values. To our knowledge, the most complete description of an atmospheric pressure argon plasma sustained by surface waves was given in Refs. [9,10]. The model provided the axial and radial structure of the surface-wave plasma column and the electromagnetic field. The model solved iteratively the mass, momentum, and energy balance equations for neutral and charged particles. Molecular ions were considered to enable the description of the discharge contraction. In this paper, we present a 2D fully coupled and self-consistent model of argon plasma at atmospheric pressure. The plasma is induced by coaxially fed microwaves under gas flow conditions. The mass, momentum, and energy balance equations for the neutral gas along with the energy balance for the electrons and the transport of excited argon atoms and atomic and molecular ions are solved to obtain the gas flow parameters as well as the spatial distributions of the gas temperature, the electron temperature, the species densities, and the electromagnetic field in the entire computational domain. The kinetic scheme accounts for elastic scattering, processes of excitation and deexcitation in collisions with electrons, direct and stepwise ionization of argon atoms, chemoionization, and production of molecular ions due to the process of ion conversion, as well as three-body and dissociative recombination due to electron and atom impact. It has been successfully applied to study deviations from thermal equilibrium in an atmospheric pressure DC torch operated in argon [11]. The scheme enables the description of the main plasma processes governing the microwave discharge under consideration. The set of partial differential equations is solved numerically using the commercial package COMSOL Multiphysics [12] based on finite-element methods. Details of the model are given, and results of calculations are discussed for discharge parameters typical for analytical applications. Experimental observations concerning the gas temperature and the electron density are presented for comparison. The calculated plasma parameters are found to be in good agreement with the experimental data available.

[*]baeva@inp-greifswald.de
[†]andre.boesel@inp-greifswald.de
[‡]ehlbeck@inp-greifswald.de
[§]loffhagen@inp-greifswald.de

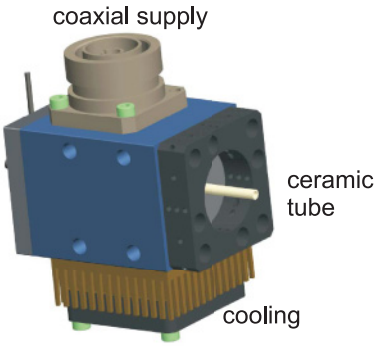

FIG. 1. (Color online) View of the MW plasma source.

II. DESCRIPTION OF THE MODEL

A side view of the compact atmospheric pressure plasma source is shown in Fig. 1. The microwave power of frequency 2.45 GHz is fed through a coaxial cable and a connector. The plasma source is operated with a forwarded power in the range from 20 to 200 W. A 2D axially symmetric schematic view of the plasma source and the computational domain are shown in Fig. 2. The microwave discharge is induced in a ceramic tube (Al_2O_3) with an inner radius of $R = 0.75$ mm and an outer radius of 1.5 mm. The length of the tube is much larger than its radius and amounts to 31.2 mm. The microwave power in the form of a TEM wave is supplied through the entrance cross section "fg" and propagates along the coaxial structure "defghj" having an inner radius of 5 mm and an outer radius of 11 mm. The argon gas is fed through the cross section "ab" with flow rates of typically 200–400 ml/min and temperature of 300 K. The model is based on the hydrodynamic approach assuming that the collision times of the particles in the plasma are much shorter than the time constants of the

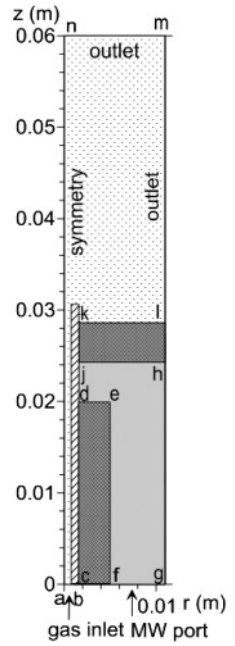

FIG. 2. Sketch of the computational domain. abklmn = fluid region, cbkb = ceramic tube, cdef = inner conductor, defghj = vacuum, hjkl = end part, outer conductor.

flow. The plasma behaves like a fluid which is considered to contain electrons and heavy particles of argon [ground state (Ar) and electronically excited atoms (Ar^*), atomic (Ar^+) and molecular (Ar_2^+) ions]. Ar^* groups the resonant and metastable 4s states of argon. The processes considered in the model are summarized in Table I. They account for elastic scattering, excitation and deexcitation, ionization by electron impact, three-body and dissociative recombination, conversion of atomic ions into molecular ions, and dissociation of molecular ions. The heavy particles are assumed to be in thermal equilibrium at a temperature T, and the electrons are characterized by a Maxwellian energy distribution function with a temperature T_e ($T_e \neq T$).

A. Microwave field equations

The electromagnetic field is described by the Maxwell equations. Assuming that the time variation of the electric and magnetic field components is harmonic and the medium is nonmagnetic, we can write

$$\vec{\nabla} \times \vec{E} = -j\omega\mu_0 \vec{H}, \quad \vec{\nabla} \times \vec{H}. = j\omega\epsilon_0\epsilon_{pl} \vec{E}. \tag{1}$$

Here ϵ_0 and μ_0 are the free space permittivity and permeability, respectively, $\vec{E}$ and $\vec{H}$ are the electric and magnetic fields, $j = \sqrt{-1}$, and ω is the angular field frequency. Introducing the light velocity in vacuum $c = 1/\sqrt{\epsilon_0\mu_0}$ and the free-space wave number $k_0 = \omega/c$, and replacing $\vec{H}$ from Eq. (1), we get

$$\vec{\nabla} \times (\vec{\nabla} \times \vec{E}) = k_0^2 \epsilon_{\rm pl} \vec{E}. \tag{2}$$

In a medium, where plasma can be present, the relative electric permittivity $\epsilon_{\rm pl}$ is given by the Lorentz formula

$$\epsilon_{\rm pl} = 1 - \frac{\omega_p^2}{\omega(\omega - j\nu_m)}, \tag{3}$$

where ν_m is the electron collision frequency for momentum transfer, $\omega_p = (\frac{n_e e^2}{\epsilon_0 m_e})^{1/2}$ is the plasma frequency, n_e denotes the electron number density, e is the elementary charge, and m_e is the electron mass. Introducing the electric conductivity

$$\sigma = \frac{n_e e^2}{m_e} \frac{1}{\nu_m + j\omega}, \tag{4}$$

and using Eq. (3), we rewrite Eq. (2) as

$$\vec{\nabla} \times (\vec{\nabla} \times \vec{E}) - k_0^2 \left(1 - j\frac{\sigma}{\epsilon_0\omega}\right) \vec{E} = 0. \tag{5}$$

Accounting for the axial symmetry and the TEM wave form, the electromagnetic field has three axially symmetric components: axial electric E_z, radial electric E_r, and azimuthal magnetic H_φ. The microwave field provides the heat source for the electrons in the plasma. The density of the absorbed microwave power is obtained from

$$Q_h = \tfrac{1}{2}\mathrm{Re}(\sigma \vec{E} \cdot \vec{E}^*). \tag{6}$$

In Eq. (6), Re denotes the real part of the corresponding expression, and $\vec{E}^*$ is the complex conjugate of $\vec{E}$.

TABLE I. List of the processes considered in the model.

j	Process	Rate coefficient K_j	$\Delta\varepsilon_j$[eV]	Reference
1	$e + \mathrm{Ar} \rightarrow e + \mathrm{Ar}^*$	$4.9 \times 10^{-15} T_e[\mathrm{eV}]^{0.5} \exp(-11.65/T_e[\mathrm{eV}])$, m^3/s	11.5	[13]
2	$e + \mathrm{Ar}^* \rightarrow e + \mathrm{Ar}$	$4.8 \times 10^{-16} T_e[\mathrm{eV}]^{0.5}$, m^3/s	-11.5	[13]
3	$e + \mathrm{Ar} \rightarrow 2e + \mathrm{Ar}^+$	$1.27 \times 10^{-14} T_e[\mathrm{eV}]^{0.5} \exp(-15.76/T_e[\mathrm{eV}])$, m^3/s	15.76	[13]
4	$e + \mathrm{Ar}^* \rightarrow 2e + \mathrm{Ar}^+$	$1.37 \times 10^{-13} T_e[\mathrm{eV}]^{0.5} \exp(-4.11/T_e[\mathrm{eV}])$, m^3/s	4.11	[13]
5	$e + e + \mathrm{Ar}^+ \rightarrow e + \mathrm{Ar}$	$8.75 \times 10^{-39} T_e[\mathrm{eV}]^{-4.5}$,$\mathrm{m}^6/\mathrm{s}$	$1.5T_e$	[14]
6	$e + \mathrm{Ar}_2^+ \rightarrow \mathrm{Ar} + \mathrm{Ar}^*$	$1.04 \times 10^{-12} (T_e[\mathrm{K}]/300)^{-0.67} \frac{1-\exp(-418/T[\mathrm{K}])}{1-0.31\exp(-418/T[\mathrm{K}])}$, m^3/s	$1.5T_e$	[15]
7	$e + \mathrm{Ar}_2^+ \rightarrow e + \mathrm{Ar} + \mathrm{Ar}^+$	$1.11 \times 10^{-12} \exp[-(2.94 - 3\frac{T[\mathrm{eV}]-0.026}{T_e[\mathrm{eV}]})]$, m^3/s	1.25	[16]
8	$\mathrm{Ar}^+ + 2\mathrm{Ar} \rightarrow \mathrm{Ar}_2^+ + Ar$	$2.25 \times 10^{-43} (T[\mathrm{K}]/300)^{-0.4}$,$\mathrm{m}^6/\mathrm{s}$		[16]
9	$\mathrm{Ar}_2^+ + \mathrm{Ar} \rightarrow \mathrm{Ar}^+ + 2\mathrm{Ar}$	$0.522 \times 10^{-15} \exp(-1.304/T[\mathrm{eV}])T^{-1}$, m^3/s		[16]
10	$\mathrm{Ar}^* + \mathrm{Ar}^* \rightarrow \mathrm{Ar}^+ + \mathrm{Ar} + e$	6.2×10^{-16}, m^3/s	$-1.5T_e$	[17]
11	$\mathrm{Ar}^* + \mathrm{Ar} \rightarrow \mathrm{Ar} + \mathrm{Ar}$	3.0×10^{-21}, m^3/s		[17]
12	$e + M \rightarrow e + M$ $(M = \mathrm{Ar}, \mathrm{Ar}^+, \mathrm{Ar}_2^+)$			[18,19]

B. Continuity and momentum equations

The fluid flow is described by the Navier-Stokes equations, which provide a solution for the total mass density ρ and the velocity field $\vec{V}$ of the mass-averaged velocity:

$$\frac{\partial \rho}{\partial t} + \vec{\nabla} \cdot (\rho \vec{V}) = 0, \tag{7}$$

$$\rho \frac{\partial \vec{V}}{\partial t} + \rho(\vec{V} \cdot \vec{\nabla})\vec{V} = \vec{\nabla} \cdot (-p\hat{I} + \hat{\tau}) + \vec{F_L}. \tag{8}$$

In Eq. (8), p is the pressure given by the sum of the partial pressures of all species, including the contribution of the electron pressure, $\hat{I}$ is the identity matrix, $\hat{\tau}$ denotes the viscous stress tensor for Newtonian fluid, and $\vec{F_L} = \frac{1}{2}\mathrm{Re}(\sigma \vec{E} \times \vec{B}^*)$ is the Lorentz force, where $\vec{B}^*$ is the complex conjugate of the magnetic induction. The mass density ρ is expressed by $\rho = M(N + n_e + N_{Ar_2^+})$ with densities of atoms $(N = N_{Ar} + N_{Ar^*})$, ions $(Ar^+, N_{Ar_2^+})$, and electrons (n_e) satisfying the Dalton's law $N = p/k_B T - n_e(1 + T_e/T)$, and the quasineutrality condition $n_e = N_{Ar^+} + N_{Ar_2^+}$. k_B is the Boltzmann constant.

C. Heavy particles' energy balance

The gas energy balance reads

$$\rho C_p \frac{\partial T}{\partial t} + \rho C_p \vec{V} \cdot \vec{\nabla} T = \vec{\nabla} \cdot (\lambda \vec{\nabla} T) + Q_{\mathrm{el}}, \tag{9}$$

where Q_{el} accounts for energy transfer from the electrons to the heavy particles. Viscous dissipation and pressure work terms have been found to play a negligible role. The thermodynamic and transport properties of the fluid such as heat capacity C_p and heat conductivity λ, are taken in the form of look-up tables as functions of the gas temperature [20,21].

D. General species equation

The equation describing the species transport in a general form reads

$$N_i \frac{\partial}{\partial t}(\ln N_i) + \vec{\nabla} \cdot [\, - D_i N_i \vec{\nabla}(\ln N_i) + N_i \vec{V}\,] = S_i. \tag{10}$$

In Eq. (10), N_i is the number density of the corresponding species, D_i is the ambipolar diffusion coefficient in case of charged species (Ar^+, Ar_2^+), and the diffusion coefficient in case of excited argon atoms. The term S_i results from reactions of production and loss of the corresponding species (see Table I). Equation (10) is solved for the dependent variable $L_i = \ln N_i$ and N_i is expressed as $N_i = \exp(L_i)$.

E. Electron energy equation

The energy conservation equation for the electron fluid has the form [14,18]

$$\frac{\partial}{\partial t}\left(\frac{3}{2} n_e k_B T_e\right) + \vec{\nabla} \cdot (\vec{F}) = Q_h - Q_{\mathrm{el}} - Q_{\mathrm{in}}, \tag{11}$$

where the flux density of the electron energy $\vec{F} = \frac{5}{2} k_B T_e \vec{\Gamma_e} - \lambda_e \vec{\nabla} T_e$ contains the hydrodynamic flux of enthalpy and the heat conduction flux. $\lambda_e = \frac{5}{2} n_e D_e$ is the electron thermal conductivity. The term Q_h describes the rate of increase of electron energy per unit volume by the electromagnetic field [see Eq. (6)]. Q_{el} is the rate of electron energy loss per unit volume as result of elastic collisions with heavy particles, and Q_{in} denotes the net rate per unit volume of inelastic energy loss from the electrons. The drift-diffusion approximation for the electron-directed velocity [22]

$$\vec{\Gamma_e} = n_e \vec{V} - \mu_e n_e \vec{E} - D_e \vec{\nabla} n_e, \tag{12}$$

and quasineutrality is assumed. Then, the electron flux can be expressed as [23,24]

$$\begin{aligned} \vec{\Gamma_e} &= -(\vec{\Gamma}_{\mathrm{Ar}^+} + \vec{\Gamma}_{\mathrm{Ar}_2^+}) \\ &= -D_{a\mathrm{Ar}^+} \vec{\nabla} N_{\mathrm{Ar}^+} + D_{a\mathrm{Ar}_2^+} \vec{\nabla} N_{\mathrm{Ar}_2^+} + n_e \vec{V} \end{aligned} \tag{13}$$

with $D_{a\mathrm{Ar}^+} = D_{\mathrm{Ar}^+} + \mu_{\mathrm{Ar}^+}/\mu_e D_e = D_{\mathrm{Ar}^+}(1 + T_e/T)$ and $D_{a\mathrm{Ar}_2^+} = D_{\mathrm{Ar}_2^+} + \mu_{\mathrm{Ar}_2^+}/\mu_e D_e = D_{\mathrm{Ar}_2^+}(1 + T_e/T)$ being the ambipolar diffusion coefficient in case of charged species (Ar^+, Ar_2^+). In the latter, the Einstein relation with ion temperatures equal to the gas temperature was applied. Equation (11) is rewritten in terms of electron energy density $\varepsilon = \frac{3}{2e} n_e k_B T_e$

in eV/m^3 as

$$\frac{\partial \varepsilon}{\partial t} + \vec{\nabla} \cdot \left\{ -\frac{5}{3}\frac{\varepsilon}{n_e}[\Sigma_j (D_{aj} - D_e)\vec{\nabla} N_j - \Sigma_j N_j \vec{V}] - \frac{5}{3} D_e \vec{\nabla} \varepsilon \right\} = (Q_h - Q_{\rm el} - Q_{in})/e \quad (14)$$

with $j = \mathrm{Ar}^+$ and Ar_2^+. Similarly to Eq. (10), Eq. (14) is solved for the dependent variables $\epsilon = \ln \varepsilon$. The right-hand side of Eq. (14) contains the net gain due to microwave heating [Eq. (6)], and losses due to elastic and inelastic collisions. The energy loss due to elastic collisions with heavy particles is obtained from

$$Q_{el} = 3\frac{m_e}{M} k_B \nu_m (T_e - T), \quad (15)$$

where the frequency for momentum transfer in elastic collisions ν_m is given by

$$\nu_m = (N_a Q_{\rm ea} + n_e Q_{\rm ei}) v_{\rm th}^e. \quad (16)$$

The cross sections for collisions of electrons with atoms $Q_{\rm ea}$ and ions $Q_{\rm ei}$, respectively, read [18,19]

$$Q_{\rm ea} = (3.6 \times 10^{-4} T_e - 0.1) \times 10^{-20} [\mathrm{m}^2] \quad (17)$$

and

$$Q_{\rm ei} = \frac{e^4}{24\pi (k_B \epsilon_0)^2} \ln \left(1.2384 \times 10^7 \sqrt{\frac{T_e^3}{n_e}} \right) \frac{1}{T_e^2} [\mathrm{m}^2], \quad (18)$$

where T_e is given in degrees Kelvin and $v_{\rm th}^e$ is the mean thermal velocity of electrons. The term $Q_{\rm in}$ accounts for energy losses due to inelastic processes (Table I), and it is expressed as

$$Q_{\rm in} = n_e \Sigma_j N_j K_j \Delta\varepsilon_j + N_{Ar^*}^2 K_{10} \Delta\varepsilon_{10}. \quad (19)$$

N_j is the number density of the corresponding species, respectively, and K_j and $\Delta\varepsilon_j$ are the rate coefficient and amount of energy loss of reaction j, respectively.

F. Heat transfer in solid

The heat transfer in the ceramic tube wall and the space between the inner and outer conductors (denoted as vacuum in Fig. 2) is described by the equation

$$\rho_s C_{ps} \frac{\partial T}{\partial t} = \vec{\nabla} \cdot (\lambda_s \vec{\nabla} T), \quad (20)$$

where ρ_s, C_{ps}, and λ_s are the mass density, the heat conductivity, and the thermal conductivity of the corresponding solid domain. In the model, the material properties for solids are assumed constant.

G. Boundary conditions

The boundary conditions of the primary variables are defined as follows. The derivatives of the particle number densities, the gas temperature, and the axial velocity along the axis of symmetry are set to zero. At the gas inlet "ab," the gas velocity has a uniform profile and a value obtained from a given flow rate (200–400 ml/min). The inflow temperature is set to 300 K. The gas pressure at the outlet cross sections "mn" and "lm" is set to 101 325 Pa. The velocity for interfaces between solid and fluid ("ak") is specified to be zero. The temperature on the metal boundaries "bdef" and "ghjkl" and on the microwave power input "fg" is set to 300 K. On the outlet, $-\vec{n} \cdot (-\lambda \vec{\nabla} T) = 0$, where $\vec{n}$ is the normal unit vector to the boundary. For the electromagnetic field, a boundary condition consistent with a perfect electric conductor (zero tangential component of the electric field) is assumed on the metallic walls, absorbing condition on the outlet part "lm," and continuous tangential components at material interfaces. At the gas inlet, the magnetic field component is set to zero. At the excitation surface "fg," and the upper open surface "mn," absorbing boundary conditions, which eliminate nonphysical reflections, are assumed [1,5,7]. Surface reactions are considered at the ceramic tube walls "ak" and the metallic surface "kl" with particle fluxes given by [25] $\vec{n} \cdot \vec{\Gamma}_j = \frac{1}{4} N_j v_{{\rm th},j}$, with $v_{{\rm th},j}$ being the thermal velocity of species j. At open boundaries we set $\vec{\nabla} N_j = 0$. The electron energy flux is set to zero along the axis of symmetry and

$$\vec{n} \cdot \vec{F} = \frac{5}{3}\frac{\varepsilon}{n_e} \vec{n} \cdot \vec{\Gamma}_e, \quad (21)$$

along material boundaries, and along open boundaries $\vec{\nabla} \varepsilon = 0$.

III. RESULTS AND DISCUSSION

Model calculations have been performed at atmospheric pressure for given gas flow rate and gas temperature (300 K) at the inlet surface "ab" and microwave power input at port "fg." Typical operating conditions for analytical applications are gas flow rates of 200–400 ml/min and absorbed microwave power of about 20 W. The calculated electric field distribution in the computational domain is shown in Fig. 3, where the field lines are presented in logarithmic scale. The schematic view of the plasma source is given again [Fig. 3(a)] with the corresponding notations for the sake of convenience. The plot in Fig. 3(b) represents the case when the plasma is still not ignited. The electromagnetic wave is guided to the upper end

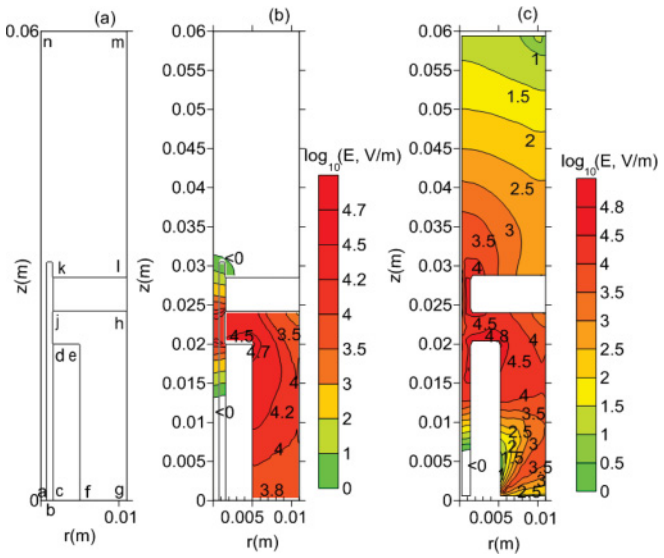

FIG. 3. (Color online) Electric field without (b) and in a presence of plasma (c) and a sketch of the computational domain (a).

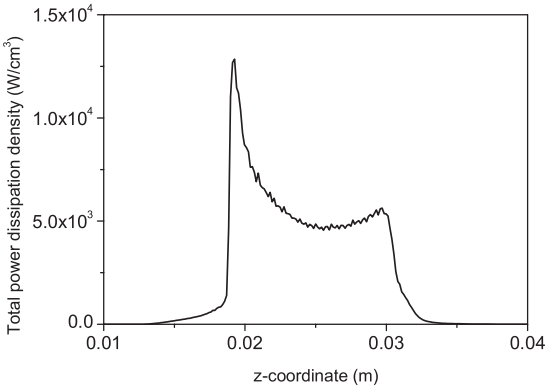

FIG. 4. Total power dissipation density along the z-axis at a gas flow rate of 200 ml/min and absorbed microwave power of 20 W.

(seen from the point of view of the sketch) of the metal source head so that almost no radiation leaves the plasma source. A maximum electric field of about 50 kV/m (for 32 W forward power) is located close to the corner "e" of the inner conductor. In front of the excitation surface "dj," the electric field has a hill-like profile along the direction of the z axis, with a maximum value of about 25 kV/m. Electromagnetic wave propagation in direction opposite to the incoming TEM wave can be seen inside the ceramic tube and tube walls. The electric field decreases by three orders of magnitude over a length of 5 mm.

In the presence of plasma [Fig. 3(c)], the electromagnetic wave is guided along the plasma boundary and propagates deeper in the computational domain in both the positive and negative direction of the z axis. Inside the tube wall, the electric field peaks twice, with maxima located on both sides of the excitation surface "dj." Inside the plasma column, the electric field decreases strongly. The power dissipation density along the z axis is shown in Fig. 4 for a gas flow rate of 200 ml/min and absorbed microwave power of 20 W. The main power in-coupling region has a length of about 13 mm. The power density reaches its maximum value upstream and decreases downstream the gas flow.

Figure 5 shows (a) the distribution of the axial component V_z of the flow velocity and the gas temperature T along the z axis, as well as (b) the spatial distribution of the gas temperature in the entire computational domain is depicted for a gas flow rate of 200 ml/min and absorbed microwave power of 20 W. The gas temperature increases in z direction from 300 K at the gas inlet to about 2130 K in the plasma region, where the temperature reaches its plateau. The axial distribution of the temperature is steeper in the upstream and shallower in the downstream direction. Accordingly, the flow is accelerated to velocities of about 11 m/s in the forepart part of the ceramic tube (the upper part in the picture view). The gas temperature and the axial velocity of the plasma jet outside the tube decrease monotonically, while the radial distribution is broadened. In the small recirculation area close to the upper end of the tube, the gas temperature increases to about 900 K.

The corresponding spatial distributions of the charged particles Ar^+ and Ar_2^+ and of the excited argon atoms are shown in Fig. 6. The microwave comes through between axial positions with coordinates $z = 0.02$ and 0.0242 m. The plasma

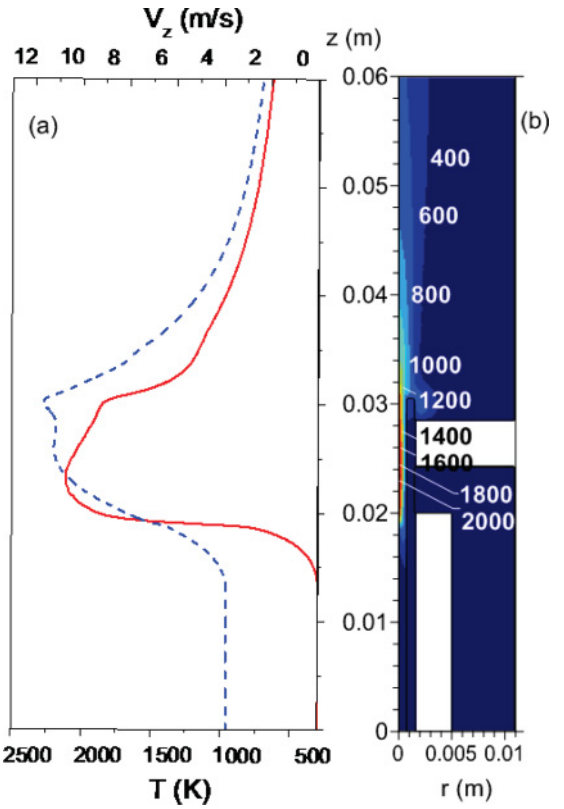

FIG. 5. (Color online) (a) Axial flow velocity V_z (dashed) and gas temperature T (solid) along the z axis, and (b) 2D plot of the gas temperature distribution at a gas flow rate of 200 ml/min and absorbed microwave power of 20 W.

column extends over a length that exceeds by a factor of about 3 to 4 the length of the excitation area, corresponding to the propagating microwave field (Fig. 3, right part). The atomic ions [Fig. 6(a)] are distributed mainly around the axis, while the distribution of their density along the axis of symmetry is asymmetric and peaked around $z = 0.0175$ m. There it reaches a value of about 4×10^{21} m^{-3}. The distribution is bell shaped in the radial direction with density decreasing by an order of magnitude within a distance of 0.4 mm. Until about halfway in the tube radius, quasineutrality is essentially preserved by the atomic ions. Beyond the molecular ion density [Fig. 6(b)] grows and becomes larger than the atomic ion density, reaching its maximum value of about 8×10^{19} m^{-3}.

The density of the excited atoms [Fig. 6(c)] demonstrates a behavior similar to that of the molecular ion density, with a maximal value of about 7.3×10^{20} m^{-3}, reached in the upstream part of the plasma region. In the recirculation region, an enhancement of the molecular ion density as well as of the density of the excited atoms is observed.

In order to explain this behavior, the radial distributions of the densities of charged particle and of the gas temperature at $z = 0.025$ m are considered in Fig. 7. This figure demonstrates the nonlinear dependence of the molecular ion density from the gas temperature. Above gas temperatures of about 1200 K, the molecular ion density is significantly lower than the atomic ion density due to the electron impact dissociation of Ar_2^+ (process 7) and the dissociative recombination of the molecular ion (process 6) in collisions with electrons. The excited atoms

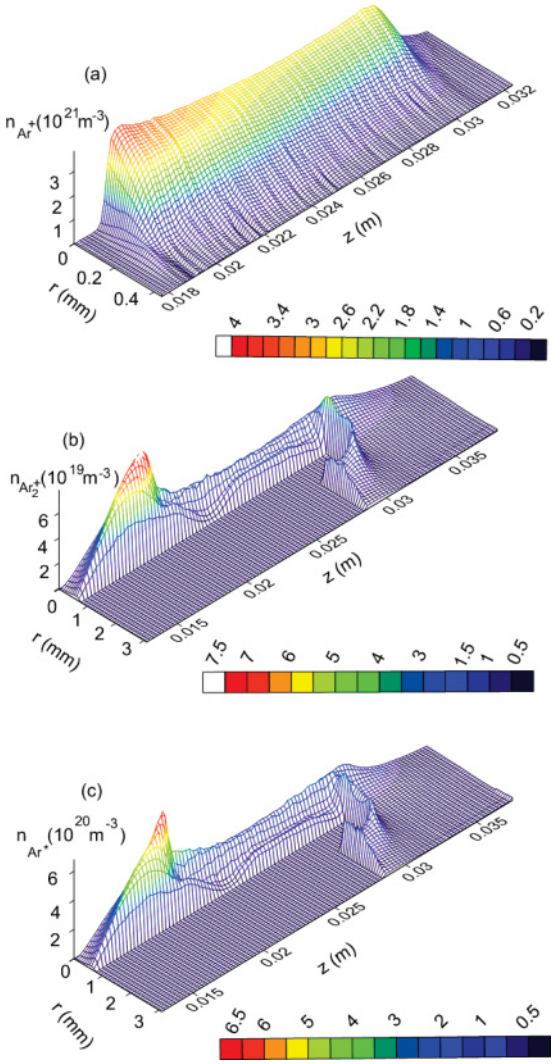

FIG. 6. (Color online) Spatial distributions of the atomic ion density (a), the molecular ion density (b), and the excited atom density (c) for a gas flow rate of 200 ml/min and absorbed microwave power of 20 W.

produced by the latter process contribute additionally to the production of atomic ions due to chemoionization (process 10), which occurs in the central plasma region. Toward the

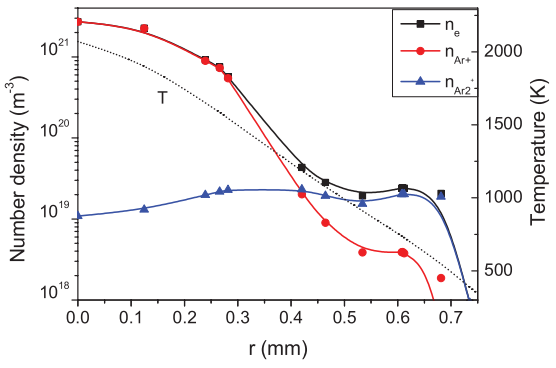

FIG. 7. (Color online) Radial distribution of the charged particle densities (solid lines with symbols) and the gas temperature (dashed curve). Cut at axial position $z = 0.025$ m. Operating conditions: gas flow rate 200 ml/min, absorbed microwave power 20 W.

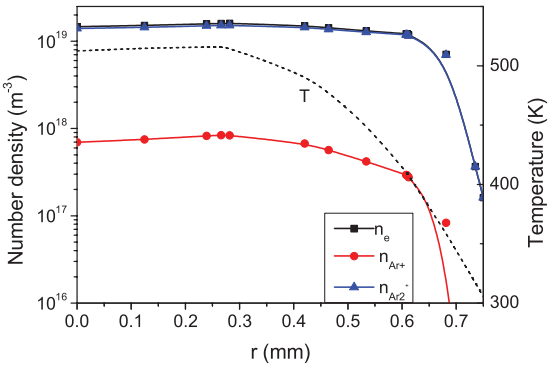

FIG. 8. (Color online) Radial distribution of the charged particle densities (solid lines with symbols) and the gas temperature (dashed curve). Cut at axial position $z = 0.025$ m. Operating conditions: gas flow rate 200 ml/min, absorbed microwave power 2 W.

tube wall, however, the gas temperature decreases and the molecular ion density increases as a result of the process of ion conversion (process 8) and the larger neutral atom density. For temperatures of about 1200 K, the molecular and atomic ion densities become almost equal; however, near the walls, where the temperature gradients are steep, the molecular ion density becomes the dominant ionic species. Similarly, for positions characterized by temperatures below 1200 K, i.e., near the edges of the plasma column, the molecular ion density exceeds the atomic ion density [Fig. 6(a)].

In order to study the impact of the plasma parameters in more detail, the gas flow rate and the absorbed microwave power, which are directly related to the gas temperature, are varied. By reducing the absorbed microwave power to 2 W, while keeping the gas flow rate constant at 200 ml/min, a maximum gas temperature of about 530 K is obtained. The radial distributions of the gas temperature, and the densities of charged particles are shown in Fig. 8. The molecular ions dominate the overall balance of charged particles in the entire plasma region in contrast to the case considered above. This behavior results from the reaction kinetics and the characteristic temperature values. The atomic ions are efficiently converted to molecular ions. The rate of production of atomic ions in reactions of electron impact dissociation of molecular ions is just about of the half of the rate of conversion.

In what follows, the proportionality assumption of Ar^+ and Ar_2^+ ion densities which was used in Eq. (13) and its validity for the present model is briefly discussed. The proportionality assumption is strongly valid for the fundamental mode of diffusion [24]. This is roughly the case if one considers the radial distribution of the electron density (Fig. 7). The ion densities demonstrate a deviation from it in their profiles. An enhancement in the ion densities close to the tube wall is observed which results from the chemoionization (process 10). Since the ambipolar electric field in the active discharge zone is mainly determined by the electrons [23], the error in the discharge model can be considered as small. Notice also that a logarithmic representation for the number densities was used in Figs. 7 and 8 to enable more plot details. Moreover, a detailed consideration of the source terms in Eq. (10) for Ar^+ resulting from the plasma reactions and the loss terms due to diffusion shows that the maximum contribution of the diffusion

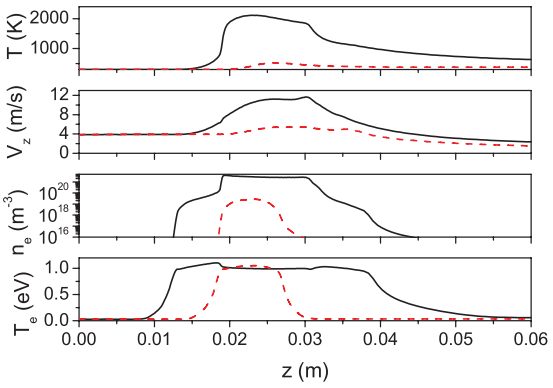

FIG. 9. (Color online) Comparison of plasma and flow parameters along the z axis for gas flow rate 200 ml/min and absorbed microwave power 2 W (dashed curves) and 20 W (solid curves).

losses of about $4\times10^{24}\,\mathrm{m^{-3}\,s^{-1}}$ appears at radial position $r = 0.3$ mm, and it is more than two orders of magnitude smaller as compared to the value of $1\times10^{27}\,\mathrm{m^{-3}\,s^{-1}}$, which corresponds to the total losses due to ion conversion (process 8) and recombination (processes 5). For the ion Ar_2^+, the diffusion loss term has a maximum of about $2\times10^{23}\,\mathrm{m^{-3}\,s^{-1}}$ near $r = 0.65$ mm, which is significantly lower than the value of $1\times10^{26}\,\mathrm{m^{-3}\,s^{-1}}$ representing the losses due to processes 6 and 7. In the low-power case (Fig. 8), the diffusion losses are also more than two orders of magnitude smaller than the corresponding collisional losses mentioned above.

A comparison of the axial distributions of the gas temperature, the axial flow velocity, the electron density, and the temperature for absorbed microwave power of 2 and 20 W is shown in Fig. 9. The profiles along the z axis are asymmetric: steep upstream and shallower downstream the gas flow. Note that even for the lower value of the in-coupled microwave power the maximum electron number density of about $2.5\times10^{19}\,\mathrm{m^{-3}}$ is well above the cutoff value $7.4\times10^{16}\,\mathrm{m^{-3}}$ corresponding to the field frequency of 2.45 GHz cutoff value. The mean electron temperature along the z axis is about 1.04 eV for absorbed power of 2 W being slightly higher than for 20 W due to the lower electron density.

The 2D spatial distribution of the electron number density is presented in Fig. 10 as a contour plot for the cases of absorbed microwave power of 2 (a) and 20 W (b). In the low-power case, the discharge fills the tube in radial direction, whereas it is constricted for the 20 W case. Consequently, the part of the total power dissipation corresponding to the central part of the plasma ($r \leqslant R/2$) is 0.55 for a total power dissipation of 20 W, whereas it is just 0.25 in the case of absorbed power of 2 W.

As is shown in Fig. 11, an increase of the gas flow rate from 200 ml/min up to 400 ml/min while keeping the in-coupled power level constant results in reduction of the maximum temperature by about 250 K. The plasma region shrinks downstream the gas flow, while the axial profiles of the gas temperature and axial component of the velocity become more extended. The in-coupling of microwave energy into the plasma, the distribution of the electron density and the gas temperature and the gas flow are involved in a complex interplay between each other. The increase of the gas flow

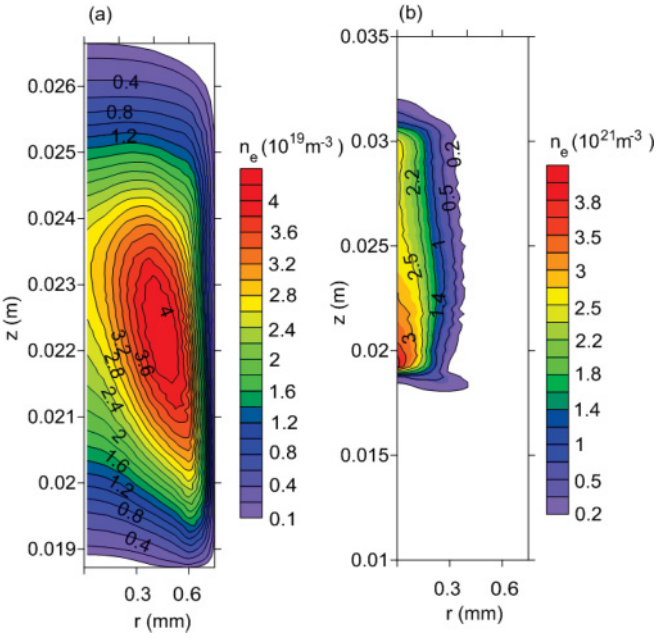

FIG. 10. (Color online) 2D spatial distribution of the electron density for absorbed microwave power of 2 W (left-hand side) and 20 W (right-hand side). Gas flow rate in both cases is 200 ml/min.

rate from 200 to 400 ml/min leads to a certain broadening of the plasma in the radial direction so that the amount of absorbed microwave power can be maintained at the same level although the plasma length is decreasing. Thereby, the plasma contraction is still evident. At the same time, the gas temperature is lower, which affects the total atom density and the rates of the chemical processes. These in turn determine the gas heating resulting from elastic collisions with electrons. Consequently, the gas flow velocity has values that ensure conservation of the mass flow.

IV. COMPARISON WITH EXPERIMENTS

Optical emission spectroscopy was applied in order to measure the average electron density and gas temperature. In the following, main aspects of the experimental procedure

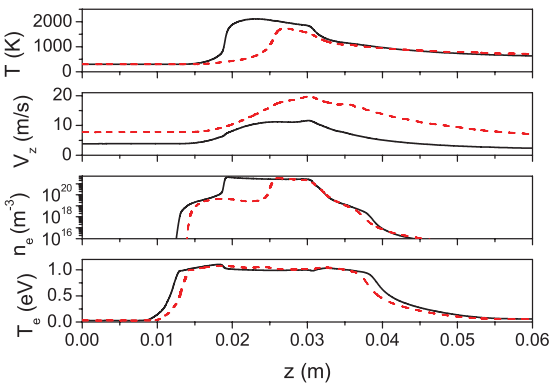

FIG. 11. (Color online) Comparison of plasma and flow parameters along the z axis absorbed microwave power 20 W and for gas flow rate 200 ml/min (solid curves) and 400 ml/min (dashed curves).

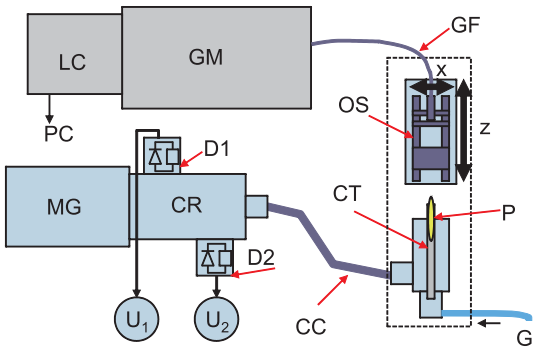

FIG. 12. (Color online) Experimental setup. LC = line camera, GM = grating monochromator, GF = glass fiber, OS = optical system, P = plasma, CT = ceramic tube, D1, D2 = diodes, CR = circulator, MG = magnetron, CC = coaxial cable, G = gas flow.

are given, and results of the comparison between experiment and model are reported.

The experimental setup is shown in Fig. 12. The radiation from the plasma is collected using an optical system (OS), which consists of two achromatic lenses ($f = 99.6$ mm) for visible light, an aperture of 15 mm diameter, a nontransparent plate of 10 mm diameter, and a further aperture of 20 μm diameter placed in the image plane of the lenses. From the image plane, the plasma radiation is conducted through an optical fiber (GF) to a 50 cm Czerny Turner spectrograph (GM) with a 2400 lines/mm grating. The entrance slit of 100 μm enables a spectral resolution of 0.09 nm. Directing this system along the z axis allows for spatial resolution of about 0.5 mm in the axial and 50 μm in the radial direction. The optical system can be adjusted in z direction by a stepper motor and translated manually in the perpendicular direction by a movable mounting.

The electron density was determined from the Stark broadening of the H_β line at 486.1 nm. The line broadening of H_β due to the linear Stark effect can be related to the electron density according to Ref. [26]. Hydrogen atoms were provided in the discharge by introducing water vapor into the carrier gas in such a small amount that the line emission of Ar does not change. The experimentally observed Stark broadening

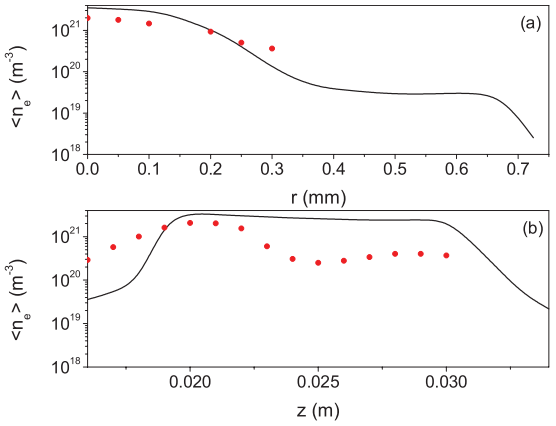

FIG. 13. (Color online) Comparison of experimental and calculated averaged electron density along the z axis. Absorbed microwave power 20 W, gas flow rate 200 ml/min.

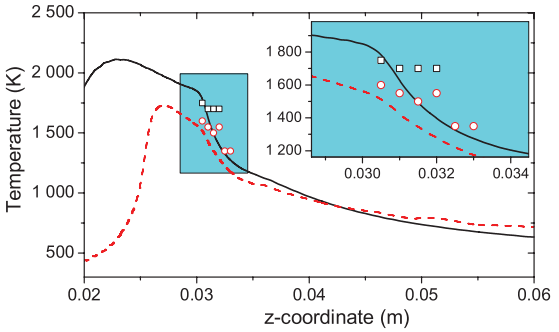

FIG. 14. (Color online) Comparison of measured (symbols) and calculated (line) gas temperature along the z axis. Absorbed microwave power 20 W, gas flow rate 200 ml/min (solid line, rectangles), and 400 ml/min (dashed line and circles).

was determined by unfolding the recorded line profile from the Doppler, the instrumental broadening, and the van der Waals broadening. In order to obtain a radial distribution of the electron density, the optical system was adjusted for various axial and radial positions in the plasma region. A drawback of this "top view" arrangement is the large background. Since temperature measurements in the plasma region were not available, the evaluation of the van der Waals broadening was done using temperature values from the model. Furthermore, in order to account for the limited spatial resolution of the experiment, the results from the model were averaged within a cylindrical volume of radius 50 μm along the z axis, and a ring of thickness 50 μm in the radial direction.

Figure 13 present the electron density obtained as a function of the radial position r at $z = 0.02$ m (a) and the axial position z (b). It can be seen that the maximum values agree within 40%. In the axial direction downstream the gas flow, the experimental values are lower by about a factor of six. This is the region close to the upper end of the tube and outside, where the deviations from axial symmetry in the experiment become considerable.

The gas temperature has been determined from the OH emission spectra from the transition $OH(A^2\Sigma^+, v = 0) \rightarrow OH(X^2\Pi^+, v' = 0)$ at 306.3 nm. Indeed, the rotational temperature of the OH radical can be assumed to represent the gas temperature; i.e., the OH radicals are in collisional equilibrium with the carrier gas. The measurements in the plume of the plasma jet have been performed looking perpendicular to the z axis and using a single quartz lens. In this "side view" arrangement, the background emission is low, at the cost of a weaker signal due to the measurement in the plasma afterglow. After excluding the background, the recorded spectra are fitted using LIFbase [27].

The results obtained for gas flow rates of 200 and 400 ml/min are presented in Fig. 14 together with the corresponding modeling results. The comparison demonstrates a good quantitative and the qualitative agreement.

V. CONCLUSION

A fully coupled 2D model of an argon plasma induced by microwave field at 2.45 GHz at atmospheric pressure has been presented. The model allows for self-consistent description of

processes of gas flow and heat transfer in the plasma source, the in-coupling of electromagnetic energy into the plasma, as well as the chemical kinetics that takes place in the plasma. The computational domain includes the region of the gas inlet, the port of the in-coming microwaves, the plasma region, where the gas is heated and the gas flow is accelerated due to the gas expansion, as well as the plume of the plasma jet. Such a description allows for a complete picture of the complex interaction between gas flow, plasma, and electromagnetic field. Since the plasma source was aimed at analytical applications, the typical operation conditions were chosen with gas flow rates of 200-400 ml/min and absorbed microwave power of 20 W. Under these conditions, the plasma was found to be far from thermodynamic equilibrium with a maximum heavy particle temperature of about 2100 K and electron temperature of about 1 eV. The electron density reaches values slightly above 4×10^{21} m^{-3}. A contraction of the discharge has been observed and explained based on the processes involved. The reaction kinetics of charged particles is related to the gas dynamics through the strongly nonlinear temperature dependence of the reaction rates. The model shows that in the plasma region, where the gas temperature comes over 1200 K, the molecular ion density is significantly lower than the atomic ion density due to the electron impact dissociation and the dissociative recombination of the molecular ions. Toward the walls and in regions, where steep temperature gradients appear, so that the gas temperature decreases rapidly below 1200 K, the molecular ion density increases due to the process of ion conversion and the higher neutral atom density. The molecular ion becomes the dominant ionic species.

Results obtained by the model are compared with experimental values from emission spectroscopy measurements, demonstrating a good agreement. The model allows for completeness of the plasma source characterization in regions where experimental observations are difficult to access.

ACKNOWLEDGMENTS

The financial support by AIF and DECHEMA (Project No. 15964BG) is greatly acknowledged.

[1] A. M. Bilgic, K. Garloff, and E. Voges, Plasma Sources Sci. Technol. **8**, 325 (1999).
[2] H. Nowakowska, M. Jasinski, and J. Mizeraczyk, Eur. Phys. J. D **54**, 511 (2009).
[3] Y. Li, M. H. Gordon, L. A. Roe, K. Hassouni, and T. Grotjohn, J. Appl. Phys. **94**, 85 (2003).
[4] C. Hunyar, E. Raeuchle, L. Alberts, R. Emmerich, M. Graf, M. Kaiser, and K.-D. Nauenburg, in *Proc. 10th Seminar Computer Modeling Microwave Power Engineering, Modena, Italy, 28–29 Feb. 2008* [http://www.wpi.edu/academics/math/CIMS/IMMG/Seminars/Past/Seminar10/program.html].
[5] S. I. Gritsinin, I. A. Kossyi, E. B. Kulumbaev, and V. M. Lelevkin, Plasma Phys. Rep. **32**, 872 (2006).
[6] V. K. Liao, M. T. C. Fang, J. D. Yan, and A. I. Al-Shammaa, J. Phys. D: Appl. Phys. **36**, 2774 (2003).
[7] L. L. Alves, R. Alvarez, L. Marques, S. J. Rubio, A. Rodero, and M. C. Quintero, Eur. Phys. J. Appl. Phys. **46**, 21001 (2009).
[8] K. Gadonna, O. Leroy, L. L. Alves, C. Boisse-Laporte, and P. Leprince, in *COMSOL Conference, Paris, France, 18–19 Nov. 2010* [http://www.comsol.com/papers/8068/].
[9] E. Castanos-Martinez, Y. Kabouzi, K. Makasheva, and M. Moisan, Phys. Rev. E **70**, 066405 (2004).
[10] Y. Kabouzi, D. B. Graves, E. Castanos-Martinez, and M. Moisan, Phys. Rev. E **75**, 016402 (2007).
[11] M. Baeva and D. Uhrlandt, Plasma Sources Sci. Technol. **20**, 035008 (2011).
[12] Comsol 4.1, [www.comsol.com].
[13] K. Makasheva and A. Shivarova, Phys. Plasmas **8**, 836 (2001).
[14] Y. P. Raizer, *Gas Discharge Physics* (Springer, Berlin, 1997).
[15] A. J. Cunningham, T. F. OMalley, and R. M. Hobson, J. Phys. B: At. Mol. Phys. **14**, 773 (1981).
[16] J. Jonkers, M. van de Sande, A. Sola, A. Gamero, A. Rodero, and J. van der Mullen, Plasma Sources Sci. Technol. **12**, 464 (2003).
[17] D. P. Lymberopoulos and D. J. Economou, J. Appl. Phys. **73**, 3668 (1993).
[18] M. Mitchner and C. H. Kruger, *Partially Ionized Gases* (Wiley, New York, 1973).
[19] S. V. Dresvin, A. V. Donskoi, V. M. Goldfarb, and V. S. Klubnikin, *Physics and Technology of Low-Temperature Plasmas* (Iowa State University Press, Ames, 1977).
[20] A. B. Murphy and C. J. Arundell, Plasma Chem. Plasma process. **14**, 451 (1994).
[21] B. Pateyron, G. Delluc, and N. Calve, Mecanique et Industries **6**, 651 (2005).
[22] P. Colella, M. R. Dorr, and D. D. Wake, J. Comput. Phys. **149**, 168 (1999).
[23] A. V. Phelps and S. C. Brown, Phys. Rev. **86**, 102 (1952).
[24] B. M. Wunderer, IEEE Trans. Plasma Sci. **6**, 406 (1978).
[25] T. Farouk, B. Farouk, D. Staack, A. Gutsol, and A. Fridman, Plasma Sources Sci. Technol. **15**, 676 (2006).
[26] H. R. Griem, *Spectral Line Broadening by Plasmas* (Academic Press, New York, 1974).
[27] J. Luque and D. Crosley, Lifbase: Database and spectral simulation (version 1.5) (2011).